Assessment of scatter for the micro-CT subsystem of the trimodality FLEX Triumph™ preclinical scanner

Daniel Gutierrez
Division of Nuclear Medicine and Molecular Imaging, Geneva University Hospital, CH-1211 Geneva, Switzerland; Geneva

Habib Zaidi[a)]
Division of Nuclear Medicine and Molecular Imaging, Geneva University Hospital, CH-1211 Geneva, Switzerland; Geneva Neuroscience Center, Geneva University, CH-1211 Geneva, Switzerland; and Department of Nuclear Medicine and Molecular Imaging, University Medical Center Groningen, University of Groningen, Groningen, The Netherlands

Purpose: This work aims at assessing, through experimental measurements and Monte Carlo calculations, the scatter to primary ratio (SPR) for the micro-CT subsystem of the FLEX Triumph™ preclinical PET-CT scanner to improve its quantitative capabilities.

Methods: Experimental measurements were carried out using the single blocker method, where five cylindrical blockers with diameters ranging between 3 and 11.65 mm were used to assess the SPR without the blocker through interpolation. Because of the vertical layout of the imaging device, the blocker was placed over rat-sized and mouse-sized phantoms and central and peripheral SPR values were obtained by rotating the source and detector. The influence of beam energy (30, 50, and 80 kVp), geometrical magnification (1.3 and 2.0) and phantom diameter (25 and 50 mm) and density (polyethylene and water) were investigated. Monte Carlo (MC) simulations using the MCNP4C code were also performed and compared to experimental results to validate their accuracy.

Results: The highest difference was found in the extreme peripheral region of the small phantom, while the maximum difference at the center of the phantom is about 6%, indicating that MC simulations can reproduce well the experimental results, at least in the region inside the phantom. The maximal SPR (0.562) was obtained for the large phantom at 30 kVp and a magnification of 1.3. The full SPR profile was calculated using MC simulations and used to express its dependency on beam energy (quadratic), air gap (asymptotic), and phantom diameter (quadratic).

Conclusions: The obtained results are in good agreement with theoretical predictions. MC simulations were valuable for the evaluation of the influence of various acquisition parameters on the SPR estimates. © *2011 American Association of Physicists in Medicine*. [DOI: 10.1118/1.3598438]

I. INTRODUCTION

Small-animal imaging has become an essential tool to study molecular pathways of disease and to test new therapeutic approaches in animal models of human disease. Preclinical PET-CT units are well established instruments in molecular imaging research as they are becoming very common. The FLEX Triumph™ system (Gamma Medica-Ideas, Northridge, CA) is one of the commercial systems offering the capability of trimodality imaging including PET, SPECT, and CT subsystems,[1] but available in many facilities as a dual-modality PET-CT system.[2]

Similar to most preclinical systems, the micro-CT unit of the Triumph™ system uses a cone-beam geometry[3] that suffers from scatter effects, which substantially reduces the quality of CT images.[4,5] This design differs from other flat pannel detectors used in mammography in the sense that it does not incorporate any scatter rejection mechanism or scatter correction technique. For this reason, it is important to characterize the amount and spatial distribution of scatter and to quantify its influence on image quality and achieved accuracy in quantitative imaging.

To assess the impact of x-ray scatter, it is important to characterize the scatter to primary ratio (SPR) of the micro-CT system. The determination of the SPR for these devices has been addressed using various experimental approaches and through computer simulations. Many studies are reported on the assessment of the scatter component in clinical CT scanners. One of the most recent works compared experimental methods to Monte Carlo simulations for a fan-beam scanner.[6] This study shows that the SPR is approximately equal to 1.034 for a 215 mm diameter phantom and tube voltage of 80 kVp, which is already high mainly because of the size of the phantom since the beam aperture at the detector is 4×50 cm^2 (64 slices). These dimensions are far from detector apertures of clinical cone-beam devices ($\sim40 \times 30$ cm^2) considering that Siewerdsen and Jaffray[4] reported an increase of the SPR of about 0.087 per degree with the increase of cone angle for a similar phantom thickness (abdomen ~180 mm). Obviously CT images are subject

to significant cupping effects that must be compensated for using either hardware scatter rejection methods (e.g., antiscatter grids) or software-based scatter correction algorithms.[5]

This issue was also investigated in the context of a preclinical PET-CT device, where the beam configuration was modified to employ a collimator allowing data acquisition using fan- and cone-beam geometries (angles of 1.336° and 12°, respectively).[7] This angle variation increased the SPR from 0.06 to 0.45 for a rat-sized phantom. Besides this work on a small-animal system, most of the SPR measurements for flat-panel detectors with similar size were made for mammographic devices. One of the most comprehensive studies related to scatter estimation on flat-panel detectors was carried out by Boone and Cooper[8] where four different experimental methods were assessed on a mammographic device. These include the evaluation of the SPR by the experimental beam-stop, scatter medium reposition, and slat methods. The same study has also compared with experimental results to Monte Carlo simulations in mammography setting, reporting SPR values up to 0.8 and for a 15 cm diameter field-of-view, 50 kVp tube voltage and phantom thickness of 6 cm. These parameters are close to the setup used on our device.

This work combines experimental measurements and Monte Carlo simulations to provide reliable estimates of the SPR on the micro-CT subsystem of the FLEX Triumph[TM] preclinical tri-modality scanner. Because of the similarity of the system configuration with the one studied by Ni et al.,[7] (i.e., vertical layout and rotation of the source and detector around the imaged object), we opted for the same experimental setup, namely the single blocker method (SBM) (Refs. 9 and 10) which demands little intervention on the system. The disadvantages of this method are that only a small part of the full SPR profile can be measured and that appropriate corrections must be applied to obtain the SPR produced by the phantom placed in the beam. For these reasons, Monte Carlo simulations using the MCNP4C code were also performed to obtain the full SPR profile with the aim to evaluate the influence of the different components on the obtained results.

II. MATERIALS AND METHODS

II.A. Micro-CT system

The commercially available FLEX Triumph[TM] preclinical PET-CT scanner (Gamma Medica-Ideas, Nortridge, CA) was used in this work.[1,2] Both PET and CT subsystems are mounted on the same gantry allowing functional and anatomical imaging without moving the animal (other than table translation). The flat-panel micro-CT subsystem is composed of an x-ray tube with an air-cooled fixed tungsten anode having a focal spot of 50 μm and an aluminium output window of 0.7 mm. The maximum tube power is 40 W with tube voltage ranging from 30 to 80 kVp. The tube current at each voltage is set by a calibration procedure, which is performed periodically. This calibration consists of data acquisition without any object in the field-of-view at three levels of exposure: (i) without any exposure to obtain the dark signal,

image, (ii) with full exposure, i.e., the highest tube current which gives an image just below detector saturation, and (iii) with half the current used in the second acquisition to verify the linear response of the detector. Data acquisition is performed automatically at the maximum exposure similar to the second acquisition of the calibration procedure.

The x-ray detector used is the Hamamatsu C7942 flat-panel sensor made of a CsI scintillator plate. It has an active area of 12×12 cm^2 with a pixel pitch of 50 μm^2 (2400×2400 pixels) and 0.15 mm thickness. The detector is protected by a 1 mm thick aluminium cover that filters the beam and render it insensitive to photons having energies below 15 keV.[11] The design of this device keeps the source to detector distance constant (SDD = 290 mm) but is able to realize a geometrical magnification (mag = SDD/SOD) by changing the source to object distance (SOD) through the displacement of the source-detector couple and leaving the object always at the center of rotation. In this way, the magnification can be set between 1.3 (SOD = 223 mm) and 2.5 (SOD = 116 mm).

II.B. Experimental phantoms

Three experimental phantoms were used to evaluate the SPR. The first is a rat-sized cylindrical polyethylene phantom with a diameter of 50 mm and a height of 250 mm. The second is a cylindrical mouse-sized polyethylene phantom with a diameter of 25 mm and a height of 250 mm whereas the third is a mouse-sized plexiglas phantom with a diameter of 25 mm and a height of 240 mm filled with water.

II.C. Single blocker method (SBM)

As mentioned earlier, the SBM was used for experimental measurement of the SPR using five cylindrical blockers of 3.0, 5.1, 7.0, 9.8, and 11.65 mm diameter. The thickness of the blockers was chosen following the calculation of the half value layer (HVL) of the highest energy beam of the micro-CT device. The beam energy refers to the effective energy (E_{eff}) corresponding to the monoenergetic beam having the same HVL as the spectrum ($\Phi_{kVp}(E)$) of the polyenergetic x-ray beam. This spectrum was generated using a simulator available in the x-ray Toolbox by Siemens[®] called *Simulation of x-ray Spectra*.[12–15] These calculations demonstrated that our 4 mm lead blockers are larger than 96 times the thickness of the HVL (0.041 mm of lead) for the highest beam energy (80 kVp) and as such they are capable to completely stop the primary beam.

The SBM was first employed by Yaffe et al.[9] and the SPR calculation method employed in this work is based on the method devised by Johns and Yaffe.[10] In this method, a first acquisition using the phantom is performed without measurement of scatter [Fig. 1(a)]:

$$M_1 = P + S = P' + P'' + S \qquad (1)$$

where M_1 is the total flux impinging on the detector consisting of the sum of the scatter produced by the phantom (S) and the primary beam (P) passing through the phantom. The primary beam is composed of P', the flux emitted by the
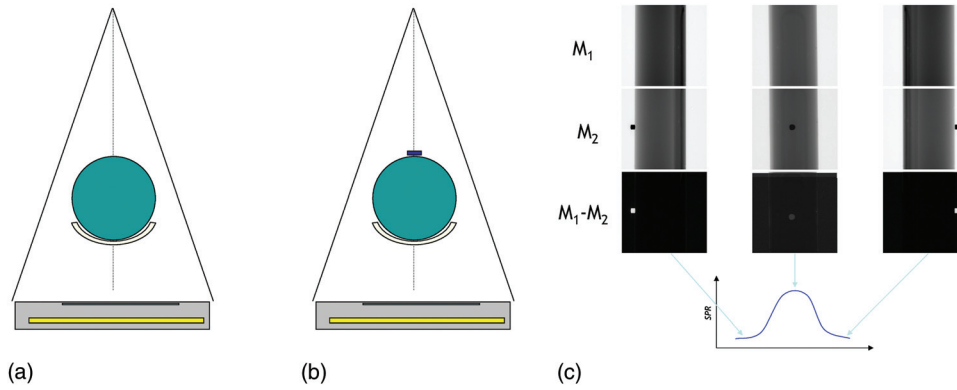
FIG. 1. Illustration of the single blocker method for scatter measurement: (a) acquisition without blocker corresponding to M_1. (b) Acquisition with blocker corresponding to M_2. (c) Blocker positions leading to derivation of the SPR central profile of the phantom.

focal spot and P'', the off-focal spot and scattered radiation produced by the filters and collimators.

A second acquisition (M_2) was performed with a lead disk positioned between the x-ray tube and the phantom that will stop the flux emitted by the focal spot P' [Fig. 1(b)]:

$$M_2 = P'' + S \tag{2}$$

To determine the primary and scatter flux, it is then necessary to estimate P''. For this purpose, Yaffe *et al.*[9] proposed a method enabling the measurement of the total flux using a third measurement (M_3) but this time without the phantom (in our case we have also removed the bed):

$$M_3 = P'_{air} + P''_{air} \tag{3}$$

where P'_{air} and P''_{air} are the focal and off-focal radiation impinging on the detector.

A fourth measurement (M_4), actually the second without the phantom, is then performed with the blocker in place to estimate the off-focal spot radiation P''_{air}:

$$M_4 = P''_{air} \tag{4}$$

The attenuation (A') in the phantom of the flux emitted by the focal spot can be estimated from the following equation:

$$A' = \frac{P'}{P'_{air}} = \frac{M_1 - M_2}{M_3 - M_4} \tag{5}$$

Analogous to the previous equation, the attenuation in the phantom (A'') of the flux emitted by off-focal radiation is defined as follows:

$$A'' = \frac{P''}{P''_{air}} \tag{6}$$

Meanwhile, it is not possible to measure this quantity as done above for A' since P'' is the unknown variable needed to calculate the SPR from Eqs. (1) and (2). To obtain P'', it is therefore necessary to calculate the ratio (RA) between off-focal radiation attenuation A'' and focal radiation attenuation A':

$$P'' = RA \cdot A' \cdot P''_{air} \tag{7}$$

This was experimentally calculated by Johns and Yaffe[10] reporting values between 0.81 and 0.89 with little apparent dependence on water pathlength (phantom thickness). For this reason, they chose a mean value of 0.86 for all conditions (Spectra from 60 to 140 kV, beam filtration of Al from 2.6 to 8.0 mm and water phantoms of 12 to 25 cm diameter). We were unable to reproduce such measurements because of the limited freedom in terms of experimental setup on the commercial preclinial PET-CT scanner. We have calculated this ratio taking into account the spectrum of the beam generated by the x-ray tube ($\Phi_{kVp}(E)$) to calculate the exponential attenuation produced by a phantom thickness x_{ph}:

$$A = \exp(-\mu(\Phi_{kV}(E)) \cdot x_{ph}) \tag{8}$$

We considered the approximation that P' spectra is equal to one of the unfiltered beam since it traverses the filters without any interaction besides photoelectric absorption of low energy photons. The second aproximation is that P'' spectra are roughly the spectrum of the filtered beam arriving after interacting with the filters. With these hypotheses, we can calculate the ratio between A'' and A' of the spectra $\Phi_{kVp}''(E)$ and $\Phi_{kVp}'(E)$, respectively. To simplify this calculation, we have replaced the spectra with their respective mean energies (Table I):

$$RA = \frac{A''}{A'} = \exp(x_{ph} \cdot (\mu(E'_{mean}) - \mu(E''_{mean}))) \tag{9}$$

To verify the accuracy of these simplified calculations, we have calculated the ratio of attenuation for a device

TABLE I. Relative attenuation (RA) calculated using Eq. (8) for two phantoms at six tube voltages as a function of their mean filtered and unfiltered energies.

Tube voltage (kVp)	30	40	50	60	70	80
Unfiltered (P') mean energy (keV)	21.50	25.97	30.12	33.90	37.38	40.80
Filtered (P'' mean energy (keV)	22.45	27.25	31.56	35.47	39.04	42.55
Water phantom (25 mm)relative attenuation (RA)	0.90	0.87	0.96	0.96	0.96	0.98
Polyethylene phantom (50 mm) relative attenuation (RA)	0.93	0.91	0.97	0.97	0.97	0.98

similar to the one described by Johns and Yaffe[10] and obtained values ranging between 0.81 and 0.90, which is in good agreement with the reported measured values.

From Eqs. (1) and (2), we obtain the SPR:

$$\text{SPR} = \frac{S}{P} = \frac{M_2 - P''}{M_1 - S} = \frac{M_2 - P''}{M_1 - (M_2 - P'')} \tag{10}$$

And from Eqs. (4), (5), (7), and (9), we can derive the SPR from the four experimental measurements:

$$\text{SPR} = \frac{S}{P} = \frac{M_2 - \text{RA} \cdot M_4 \cdot \dfrac{M_1 - M_2}{M_3 - M_4}}{M_1 - \left(M_2 - \text{RA} \cdot M_4 \cdot \dfrac{M_1 - M_2}{M_3 - M_4}\right)} \tag{11}$$

To take into account the presence of the blocker, Johns and Yaffe[10] devised a scatter reduction factor (S_B) in Eq. (1) by calculating the 1st scatter to primary ratio (S_{B1}/P) and introduced this value in the final form of Eq. (11) to correct the final result. We have followed the approach proposed by Ni et al.[7] instead to extrapolate the results of the SPR estimates obtained using the five blockers to a blocker having a diameter of 0 mm.

The device has a vertical layout (Fig. 1) and the blocker was placed directly over the phantom. For this reason, central and peripheral values of the SPR were obtained by rotating the tube-detector pair around the phantom-bed-blocker assembly [Fig. 1(c)] and the SPR profile fitted to a Gaussian function. As discussed in Sec. II F, the bed is not radio-transparent and as such we do not expect similar SPR profiles from different projections.

II.D. Monte Carlo simulations

The MCNP4C (Monte Carlo N-Particle Transport code version 4C)[16] code developed to simulate random processes associated with radiation interaction and detection was used in this study. This is a general purpose Monte Carlo package that uses continuous-energy nuclear and atomic data libraries for neutron (energies from 10^{-11} to 20 MeV), photon and electron (energies from 10^{-3} to 1000 MeV) transport. Different modes of interaction involving one, two or all three types of particles can be simulated. The code is very often used in medical physics applications particularly in the field of diagnostic imaging.[17]

The use of the MCNP code involves the creation of an input file containing information about the geometry, the materials, the location and characteristics of the source, the type of particles to be tracked, the type of desired answers and variance reduction techniques used to improve computational efficiency. The simulation geometry consists of a simplified model of the imaging device (see Sec. II A), where only photon transport was considered. The former was limited to a cylindrical box corresponding to the dimensions of the device enclosure containing its individual components, namely:

- The photon source with energies sampled from an unfiltered spectrum[18] corresponding to a tungsten anode tube taking into account additional filters,
- The phantom and the carbon fiber bed,
- The detector simulated as a multilayer of items [Fig. 2(c)] representing the detector window, the detector sub-cells and *surface source write* (SSW) or *surface source read* (SSR) cards, the order of which is changed to simulate different situations as explained in Sec. III A.

The SSW card is used to write a surface source file to be used in subsequent calculations that will be read by the SSR with the option to distinguish particles arising from a collision from uncollided particles, i.e., distinguish scatter from primary radiation.

The full gantry geometry was accurately reproduced, however, because of memory limitations and computational efficiency issues, the detector was only simulated on 61 sub-cells of $0.5 \times 0.5 \times 0.15$ mm^3 size of the full physical detector ($120 \times 120 \times 0.15$ mm^3) (Fig. 2). The placement of these sub-cells was chosen to take into account the cylindrical
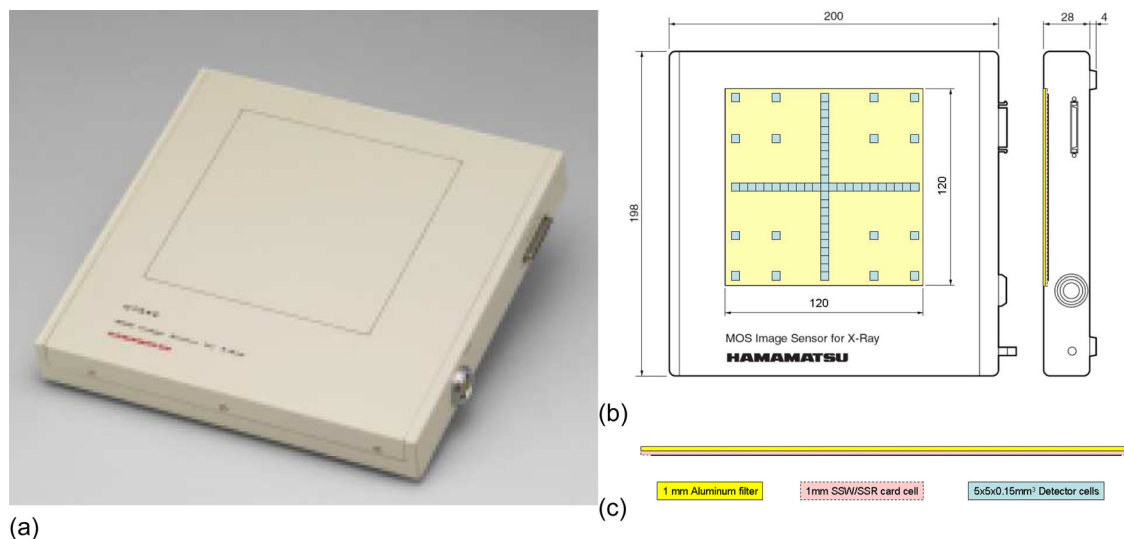

FIG. 2. (a) Photograph of the detector (courtesy of Hamamastu Photonics K.K., Japan). (b) Monte Carlo model of detector sub-cells position (blue) behind the 1 mm aluminium window superimposed on the detector diagram. (c) Drawing of the Monte Carlo simulation model of the detector geometry.

shape of the phantoms, where the results on the remaining parts of the detector were derived using bicubic interpolation. These 61 sub-cells were set to *Pulse height tallies* that provide the energy distribution of pulses created in a cell that models a physical detector to obtain the energy deposition in each cell per initial simulated particle (mega-electron-volt/particle).

II.E. Comparison between experimental and simulation results

To compare experimental single blocker and Monte Carlo simulation results, we simulated the rotation of the tube-detector assembly and calculated the SPR for different projection angles. These angles were selected, such that, they correspond to the simulated detector sub-cells as shown in Fig. 3 using the following equation:

$$p = \frac{r \cdot \sin(\alpha)}{1/\text{mag} - r \cdot \cos(\alpha)/\text{SDD}} \quad (12)$$

where r is the phantom diameter, α the projection angle, SDD the source to detector distance (always equal to 29 cm in this device), and mag (mag = SDD/SOD) the geometrical magnification.

With this rotation, we have determined the SPR profile of the central slice, which was fitted to a Gaussian function similar to the experimental measurements for comparative analysis of both methods. The comparisons were realized for five different conditions: data acquisition with a magnification of 1.3 and tube potentials of 30, 50, and 80 kVp using the 50 mm diameter phantom, acquisition with a magnification of 2.0 and a tube potential of 50 kVp and another acquisition using the 25 mm diameter phantom with a magnification of 1.3 and a tube potential of 50 kVp.

Our preliminary investigations showed a relatively high difference between experimental and MC simulation results

outside the phantom region. One possible explanation is that the calculation of the SPR using the experimental method follows a different trend inside and outside the phantom region. To better understand this behavior, we have performed four additional MC simulations (polyethylene phantom, mag. = 1.3 at 50 kVp) to track the history of primary and scatterred radiation and understand their path and influence on the final SPR results. The diagram of these additional simulations together with one of the standard simulations is shown in Fig. 4. Further explanations are given below:

(a)   *Before phantom* situation was scored by placing the SSW-SSR cards of MCNP *after* the tube filter and *before the phantom*. This will provide an estimation of the primary on and off-focal spot corresponding to particles without and with collisions, respectively (P' and P'' for the experimental measurements).

(b)   *After phantom* situation corresponds to the placement of the SSW-SSR cards just before the detector cover and *after the phantom*, to estimate the scatter produced by the phantom and the bed.

(c)   *After cover* situation is the standard simulation with the SSW-SSR cards placed *after the detector cover* and before the detector to allow the estimation of the increment of scatter produced by the detector cover when the phantom is present.

(d)   *Background before cover* situation is similar to the *after phantom situation* case (b) but this time the phantom and the bed are not present in the simulation model, thus allowing the estimation of the primary on and off-focal spot in air (P'_{air} and P''_{air} for the experimental measurements).

(e)   *Background after cover* situation is a simulation with the SSW-SSR cards located just *after the detector cover* and before the detector (as in the main
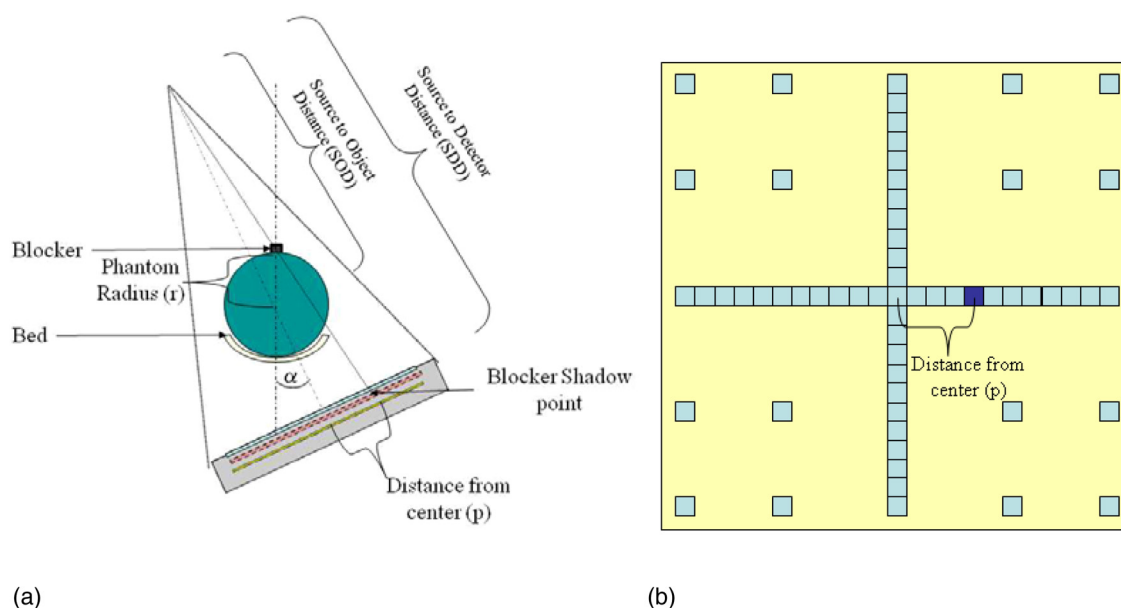

(a)

(b)

FIG. 3. (a) Drawing showing Monte Carlo simulation of the rotation of the tube-detector assembly corresponding to Eq. (12), and (b) the detector read for comparison purposes.
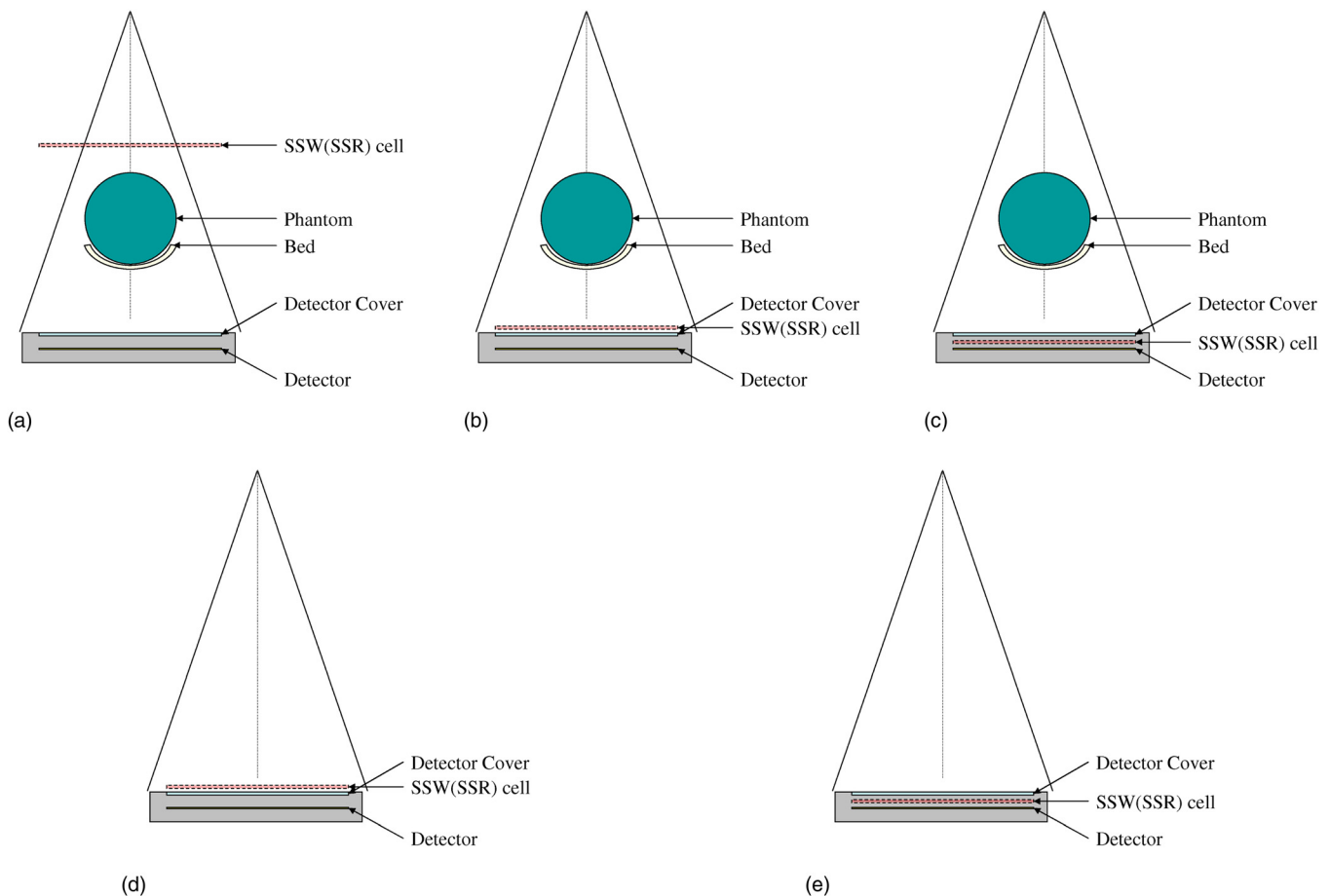
FIG. 4. Illustration of the five different MC simulation setups used to illustrate the origins of the difference between experimental and MC results: (a) before phantom, (b) after phantom, (c) after cover, (d) background before cover, and (e) background after cover.

simulations), but this time without the bed and phantom. This simulation allows the estimation of the scatter produced by the detector cover.

It should be emphasized that the experimental method described in Sec. II C, especially Eqs. (1) and (2), correct the intuitive primary measurement (M_1) by increasing the primary estimate (P') through the addition of scattered radiation mainly from the tube filter (P''), and subtracting this value from the intuitive scatter estimate (M_2) to evaluate the phantom scatter only (S). In the following example, we discuss how this correction can affect the SPR estimation on the micro-CT scanner mainly because of the presence of the aluminium cover detector.

Figure 5 shows the variation of the magnitude of primary radiation through all the previously described steps. It can be seen that the number of primary pulses received by the detector change only in the phantom region [Fig. 5(a)]. However, the energy deposited on the detector is quite different when the phantom is present in the simulation model [Fig. 5(b)]. This is better put into evidence by the increase of the energy between each step [Fig. 5(d)] since the critical step for the primary seems to be the crossing of the phantom where the change in the primary deposited energy is around

110% while the primary reduction induced by the detector cover is close to 5%. One of the plausible explanations is that the primary correction that considers all the effects of the imaging device on the primary off-focal spot (P'') is significant and dependent on the phantom position and is negligible for the detector cover regardless of the presence of the phantom.

By analyzing the scatter variation, one can observe in Fig. 6 that the scatter pulses produced before the phantom (P'') are quite small to arrive until the detector [Fig. 6(a)], not only because of the distance but also probably because of the detector cover. It can also be seen that the scatter produced on the phantom represents most of the scatter energy impinging on the detector [Fig. 6(b)]. This can be clearly noticed when comparing the scatter energy increase at each step of the beam interaction [Fig. 6(d)] since this increase is about 190% in the phantom region and 150% outside the phantom region.

What is important to notice in this part is that while the influence of the detector cover on the primary beam is low (5%) and insensitive to the presence of the phantom, this is not the case for the scatter because the cover increases the scatter by ∼10% in the phantom region and ∼5 times more outside the phantom region probably because of the high amount of primary arriving to this region. This amount
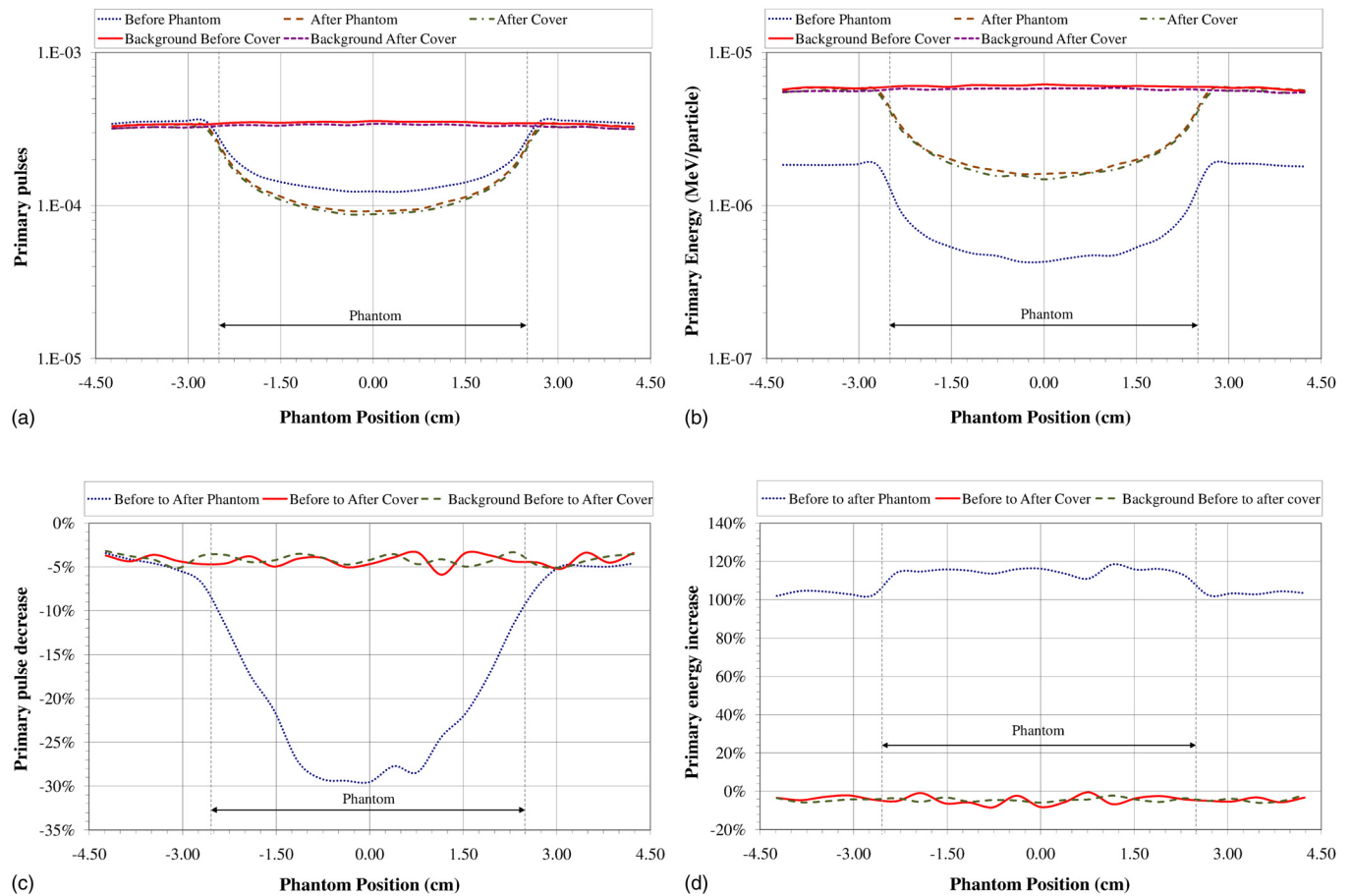
FIG. 5. Variation of the magnitude of primary radiation at different positions of the micro-CT scanner. Primary (a) pulses and (b) energy captured in the detector normalized by the number of starting particles. Relative primary (c) pulses decrease and (d) energy increase for each step of the simulation.

cannot be estimated experimentally. This sensitivity to the phantom presence explains the good agreement between MC simulations and experimental results in the phantom region while in the outer part, the scatter is either underestimated by the experimental method and/or overestimated by the MC simulations.

II.F. Influence of the carbon fibre bed

The rotation of the bed was simulated to reproduce the rotation of the tube-detector assembly to assess the influence of the bed on the SPR magnitude and spatial distribution during a standard CT acquisition. The SPR for seven projection angles ranging between 0° and 90° with a step of 15° was obtained.

Figure 7 shows a diagram of the bed position relative to the tube-detector assembly for four simulation conditions together with a bicubic interpolation of the corresponding 2D SPR. During this rotation, the maximum SPR slowly decreased from 0.47 for the projection at 0° to 0.41 for the projection at 90°. The position of this maximum has also changed from the central point to a point located ~1 cm away from the center of the detector in the direction of the bed position. The precision of this displacement could not be better defined because of the size of the simulated detector sub-cells. In agreement with results reported elsewhere by Men *et al.*[19] our results demon-

strate that the bed is responsible of a nonnegligible amount of scatter generated by the micro-CT device which should be considered when correcting CT images for scattered radiation.

III. RESULTS AND DISCUSSION

III.A. Experimental measurements and comparison with Monte Carlo simulations

SPR results obtained at three different tube potentials are shown in Fig. 8(a), where marker points represent experimental measurements for an angle position of tube-detector couple whereas curves represent Gaussian fits to the data. One can observe that the highest SPR (0.540) is obtained with a tube potential of 30 kVp while the SPR for the two other tube potentials (50 and 80 kVp) are quite similar (0.444 and 0.452, respectively).

Monte Carlo simualtion results are shown in Figs. 8(b)–8(d), where marker points represent simulation results of a tube-detector angle and the corresponding sub-cell detector defined by Eq. (12), whereas curves represent their Gaussian fit. Overall, there is a good agreement between experimental and Monte Carlo simulation results at least in the region corresponding to the phantom size, since the mean relative difference between the two methods is below 2.5% for the
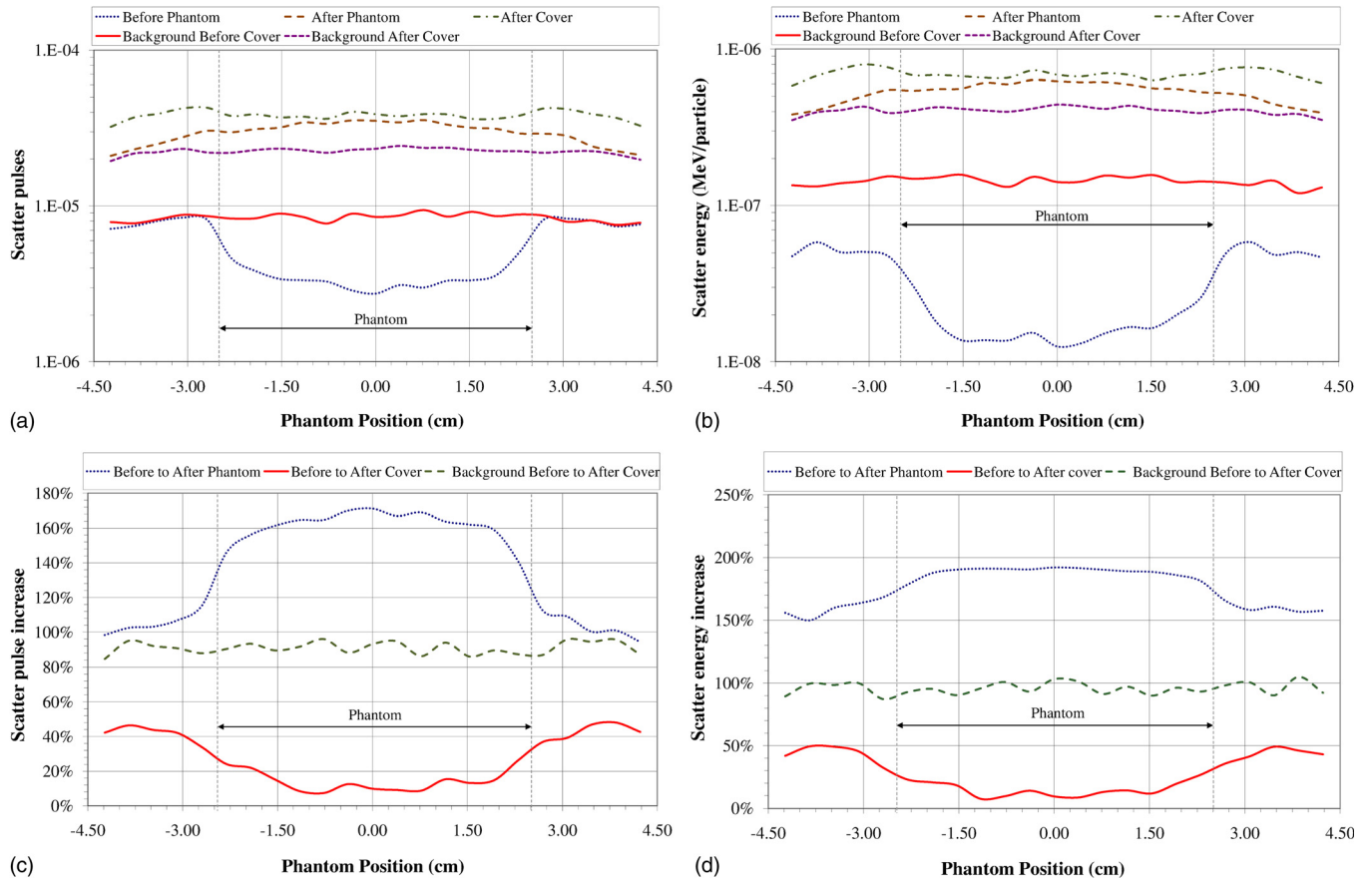
FIG. 6. Variation of the magnitude of scattered radiation evolution at different positions of the micro-CT scanner. (a) Scatter pulses and (b) energy captured in the detector normalized by the number of starting particles. (c) Relative scatter pulses and (d) energy increase for each step of the simulation.
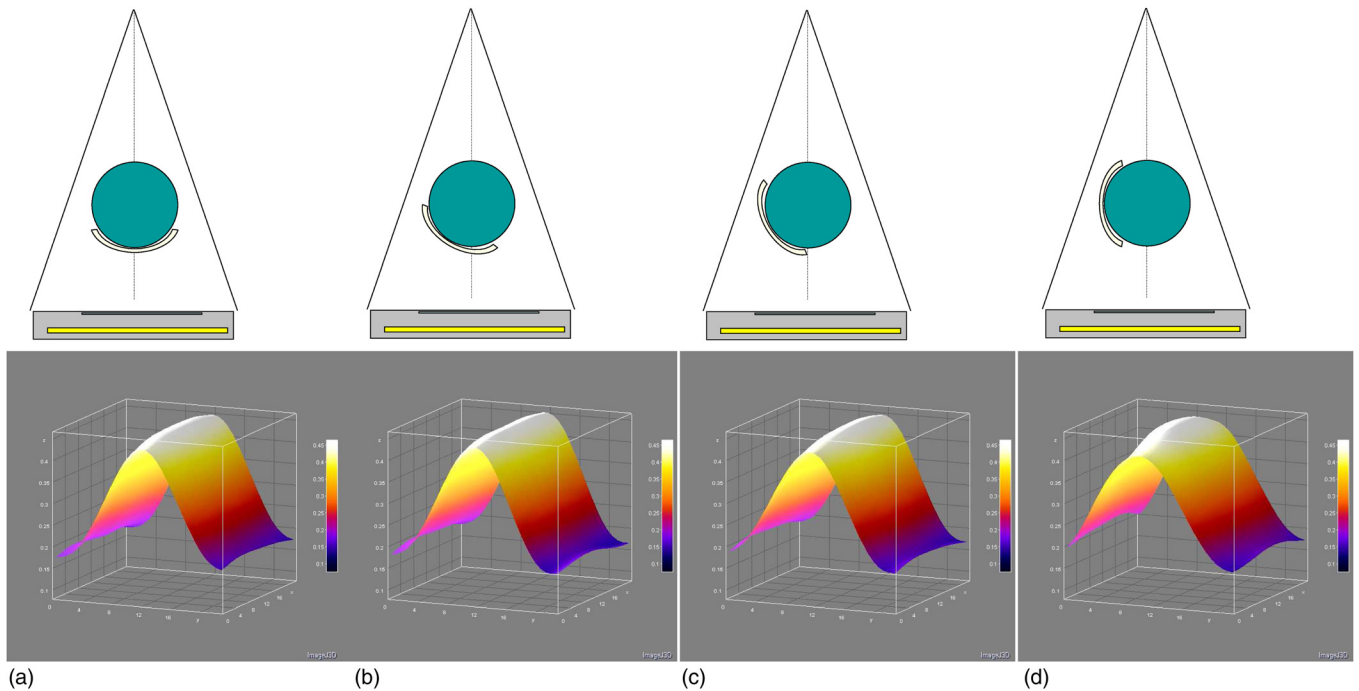

FIG. 7. Influence of the bed on the SPR magnitude and spatial distribution. Diagram representing the position of the bed coupled to the result of the 2D bicubic interpolation representing the SPR distribution at the detector. Bed position at a projection angle of: (a) 0°, (b) 30°, (c) 60°, and (d) 90°.
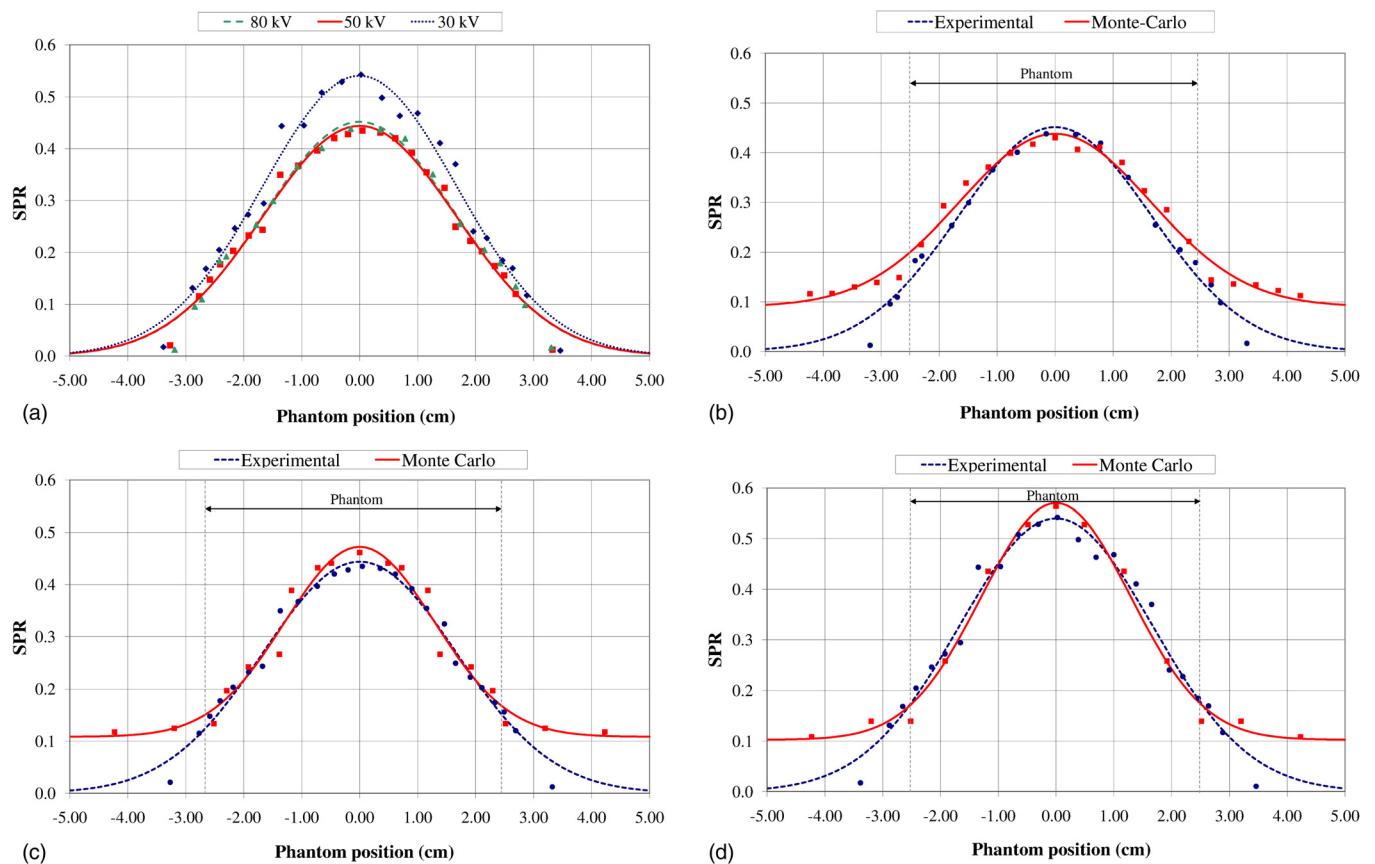
FIG. 8. SPR at different phantom (φ50 mm) positions as a function of tube potential for a magnification of 1.3. Data points represent experimental or simulation results while curves represent Gaussian fits. (a) Experimental results for tube voltages of 30, 50, and 80 kVp. Comparison between experimental measurements and Monte Carlo simulations for: (b) 80 kVp, (c) 50 kVp, and (d) 30 kVp.

three situations. The difference at the maximum SPR is below 6% and increases in the phantom's peripheral region.

The SPR obtained with the 50 mm diameter phantom and a magnification of 2.0 is shown in Fig. 9(a). As expected, the SPR decreases with magnification because of the increase of the air gap and the reduction of the exposed region in the phantom. The comparison again shows that the MC model predicts well the results obtained on the experimental setup [Fig. 9(b)] since the relative difference at the central point is below 1%.
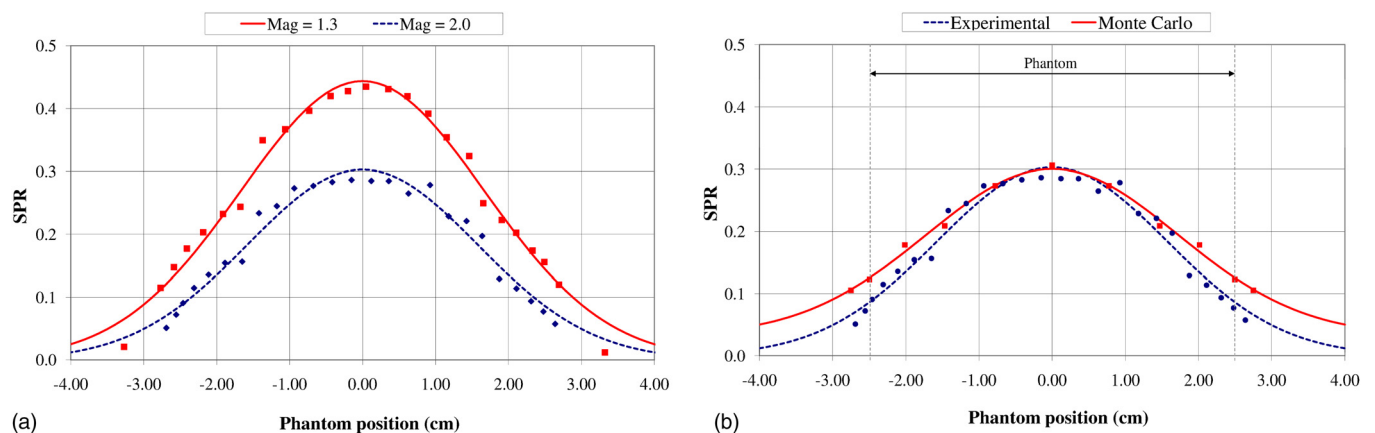
However, it increases at the peripheral part of the phantom giving a mean difference of 9.35% in the phantom region.

The influence of phantom size on SPR is shown in Fig. 10(a) for a polyethylene phantom of φ25 mm at a tube voltage of 80 kV. The experimentally obtained SPR is 0.208 at the center of the phantom and is noticeably lower than the measured SPR (0.452) for a 50 mm diameter phantom. Similar to all comparative evaluation results between experimental measurements and MC simulations [Fig. 10(b)], the

FIG. 9. SPR at different phantom (φ50 mm) positions as a function of geometrical magnification at 50 kVp where data points represent experimental or simulation results while curves represent Gaussian fits. (a) Experimental results for magnifications of 1.3 and 2.0. (b) Comparison between experimental measurements and Monte Carlo simulations for a magnification of 2.0.
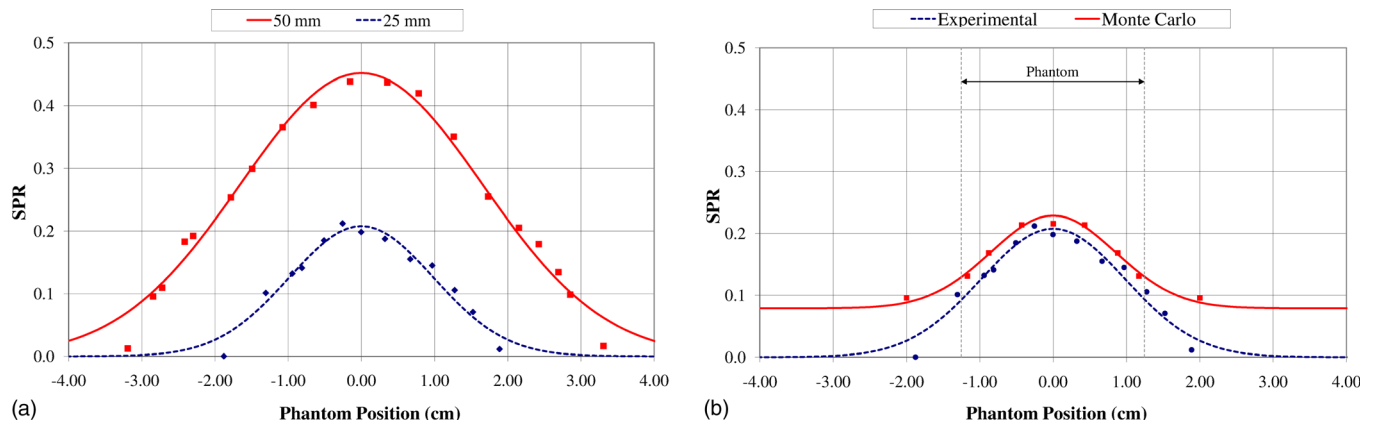
FIG. 10. SPR at different phantom positions as a function of phantom size. Data points represent experimental or simulation results while curves represent Gaussian fits. (a) Experimental results for φ50 mm and φ25 polyethylene phantoms. (b) Comparison between experimental and Monte Carlo results for a φ25 mm polyethylene phantom.

difference is about 14.4% and it is especially at its center (9.24%).

Finally, the influence of phantom density on SPR is shown in Fig. 11(a) for a water phantom of φ25 mm at a tube voltage of 80 kV. The experimentally obtained SPR is 0.275 at the center of the phantom and is higher than the one measured using the polyethylene phantom of the same size (0.208). MC simulations [Fig. 11(b)] show a relatively low difference inside the phantom region (<11.2%), again especially at its centre (<5%).

The results are summarized in Table II where experimental and simulation results of the SPR at the central phantom point are shown together with relative differences between the two approaches at the same central point and as a mean inside the region corresponding to the phantom's size. It is obvious that higher relative differences are noticed when the global SPR is lower as is the case for a magnification of 2.0 and with smaller phantoms.

III.B. Influence of acquisition parameters on the SPR

Following the methodology described by Chen et al.,[20] the variation of the maximum SPR value as a function of the various acquisition parameters was assessed using MC simulations. The first test was made by simulating a 50 mm diameter polyethylene phantom with a magnification of 1.3 realized by changing the beam spectra of our simulation to obtain tube voltages ranging from 30 to 80 kVp with a step of 10 kV. Figure 12 shows that the variation of the maximum SPR can be fitted with a quadratic polynomial function giving a theoretical minimum SPR for a voltage of ~77.5 kVp (effective energy ~40 keV) which is very close to the minimum experimental tube voltage (80 kVp). This can be explained by the competitive effect of energy-dependent coherent and incoherent scatterings.

The second tested parameter is the magnification, which was varied by changing the source to object distance to produce values of 1.3, 1.7, 2.0, 2.2, and 2.5 (Fig. 13). A 50 mm diameter polyethylene phantom and tube voltage of 50 kVp was simulated. Since the scatter should decrease by increasing the distance, the theoretical infinite distance should provide the minimum SPR. For this reason, we have chosen to interpolate the results with a negative power equation, which resulted in a minimum asymptotic SPR of 0.239.

Finally we have performed six additional simulations with a magnification of 1.3 and tube voltage of 50 kVp with the polyethylene phantom having diameters ranging from
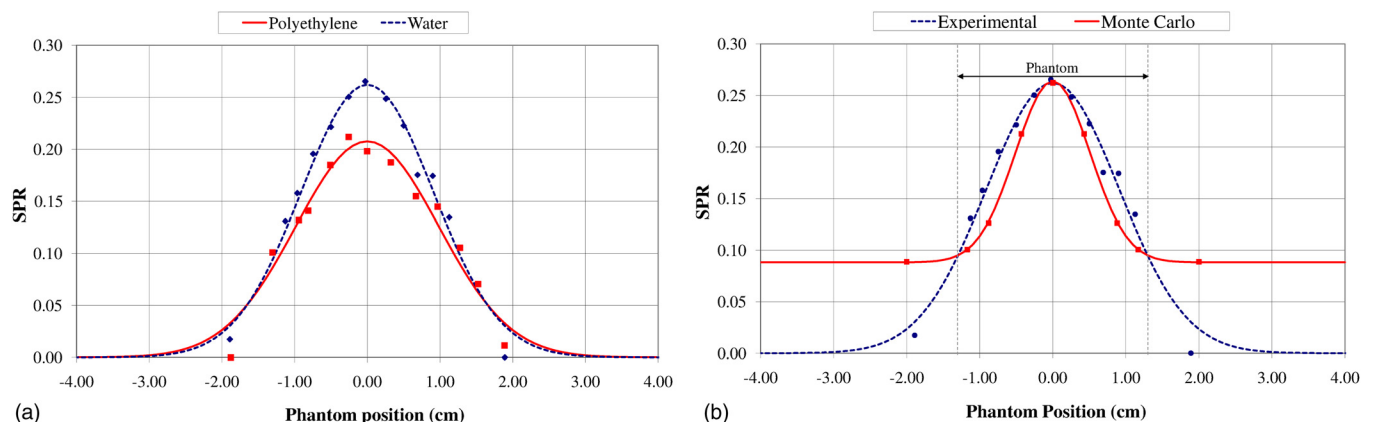

FIG. 11. SPR at different phantom positions as a function of phantom density. Data points represent experimental or simulation results while curves represent Gaussian fits. (a) Experimental results for φ25 mm polyethylene and water phantoms. (b) Comparison between experimental and Monte Carlo results for a φ25 mm water phantom.

TABLE II. Relative difference between Monte Carlo and experimental measurements of the SPR.

	Polyethylene phantom					Water phantom
	(ϕ50 mm)				(ϕ25 mm)	(ϕ25 mm)
	Mag. = 1.3			Mag. = 2.0	Mag. = 1.3	
Conditions	30 kVp	50 kVp	80 kVp	50 kVp	80 kVp	
Max. SPR (experimental)	0.540	0.444	0.452	0.303	0.208	0.275
Max. SPR (MC)	0.571	0.472	0.428	0.300	0.229	0.289
Difference @ Max SPR (%)	5.33	6.03	−2.44	−0.85	9.24	4.84
Mean difference inside the phantom (%)	−2.30	2.35	1.17	9.35	14.37	11.19

2.5 to 5.0 cm (0.5 cm step) to study the influence of the phantom size on the SPR (Fig. 14). The fitting curve is again a quadratic polynomial since the scatter increases proportionally with the irradiated volume, which in turn is proportional to the square of the phantom diameter.

Another issue that deserves particular attention is that preclinical dual-modality PET-CT imaging has important ramifications for quantification of molecular targets of normal and disease states. However, preclinical PET image quantification suffers from many physical degrading factors, one of them being photon attenuation which can be corrected for using different strategies.[21] The common technique implemented on combined PET-CT systems is CT-based attenuation correction (CTAC), which must be performed ideally using accurate and artefact-free CT images.[22,23] In future work, we plan to exploit the potential of fast Monte Carlo-based scatter modeling and correction to improve the quantitative capabilities of the micro-CT system.[23] The final objective would be to derive accurate attenuation maps for improved attenuation correction of corresponding PET data.

IV. CONCLUSION

In this work, we measured the SPR in the micro-CT subsystem of a commercial tri-modality preclinical platform and demonstrated that its magnitude is not negligible mainly because of the cone-beam geometry of the flat-panel based system design as reported previously.[7,24] We have also shown that the MCNP4C code can be used with confidence to predict the SPR of a dedicated micro-CT system and provide an estimation of the contribution of the different components involved in the production of scattered radiation. In this particular device, the detector cover is responsible for a relatively high amount of scatter mainly in those regions where primary photons impinge directly on the cover.

The MCNP4C code is capable to reproduce results of various experimental measurement conditions for this device with good confidence inside the phantom region, especially when modeling conditions producing high SPR. When the SPR is lower, the relative difference increases up to 14.4% (φ25 mm phantom) mainly because of the global SPR reduction since the absolute difference between experimental and MC simulation results is almost constant ($\sim$0.02). It was also demonstrated that the fibre carbon bed used for positioning the phantom in the micro-CT field-of-view is also responsible for a nonnegligible amount of scatter since its influence can be observed when projection data are acquired with different angles contributing to approximately 10% of the total SPR. Likewise, MC simulations were valuable for the evaluation of the influence of various acquisition parameters on the SPR estimates and can be used with confidence for the optimization of system design and acquisition and reconstruction protocols for quantitative micro-CT or combined PET-CT imaging.
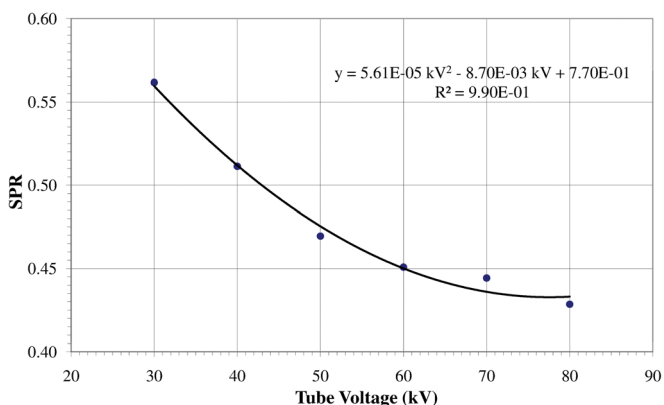
FIG. 12. Plot of the maximum SPR assessed using Monte Carlo simulations as a function of tube voltage.
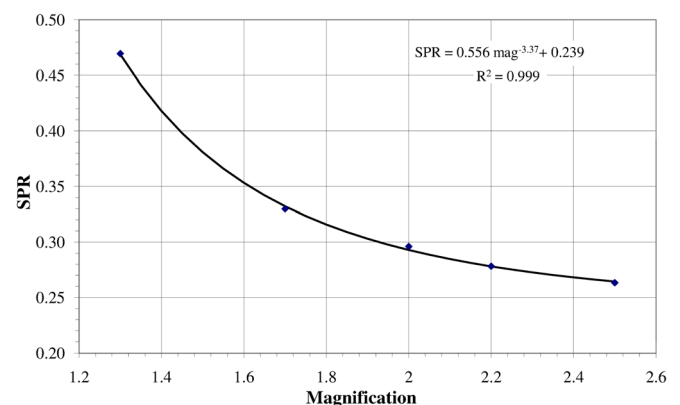
FIG. 13. Plot of the maximum SPR assessed using Monte Carlo simulations as a function of geometrical magnification.
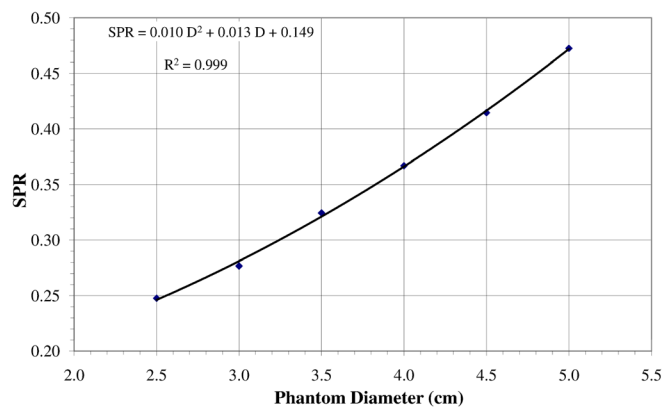
FIG. 14. Plot of the maximum SPR assessed using Monte Carlo simulations as a function of the polyethylene phantom diameter.

ACKNOWLEDGMENT

[a] Author to whom correspondence should be addressed. Electronic mail: habib.zaidi@hcuge.ch, Telephone: +41 22 372 7258; Fax: +41 22 372 7169.

[1] K. B. Parnham, S. Chowdhury, J. Li, D. J. Wagenaar, and B. E. Patt, "Second-generation, tri-modality pre-clinical imaging system," IEEE Nucl. Sci. Symp. Conf. Rec. 3, 1802–1805 (2006).

[2] R. Prasad, O. Ratib, and H. Zaidi, "Performance evaluation of the FLEX Triumph^{TM} X-PET scanner using the NEMA NU-04 standards," J. Nucl. Med. 51, 1608–1615 (2010).

[3] L. R. MacDonald et al., "Evaluation of x-ray detectors for dual-modality CT-SPECT animal imaging," Proc. SPIE 4786, 91–102 (2002).

[4] J. H. Siewerdsen and D. A. Jaffray, "Cone-beam computed tomography with a flat-panel imager: Magnitude and effects of x-ray scatter," Med. Phys. 28, 220–231 (2001).

[5] R. Gupta et al., "Ultra-high resolution flat-panel volume CT: Fundamental principles, design architecture, and system characterization," Eur. Radiol. 16, 1191–1205 (2006).

[6] A. Akbarzadeh, M. R. Ay, H. Ghadiri, S. Sarkar, and H. Zaidi, "Measurement of scattered radiation in a volumetric 64-slice CT scanner using three experimental techniques," Phys. Med. Biol. 55, 2269–2280 (2010).

[7] Y. C. Ni et al., "Magnitude and effects of X-ray scatter of a cone-beam micro-CT for small animal imaging," Nucl. Instrum. Methods A 569, 245–249 (2006).

[8] J. M. Boone and V. N. Cooper, "Scatter/primary in mammography: Monte Carlo validation," Med. Phys. 27, 1818–1831 (2000).

[9] M. Yaffe, A. Fenster, and H. E. Johns, "Xenon ionization detectors for fan beam computed tomography scanners," J. Comput. Assist. Tomogr. 1, 419–428 (1977).

[10] P. C. Johns and M. Yaffe, "Scattered radiation in fan beam imaging systems," Med. Phys. 9, 231–239 (1982).

[11] N. Yagi, M. Yamamoto, K. Uesugi, and K. Inoue, "A large-area CMOS imager as an X-ray detector for synchrotron radiation experiments," J. Synchrotron Radiat. 11, 347–352 (2004).

[12] https://w9.siemens.com/cms/oemproducts/Home/XrayToolbox/spektum/Pages/Default.aspx.

[13] J. M. Boone, T. R. Fewell, and R. J. Jennings, "Molybdenum, rhodium, and tungsten anode spectral models using interpolating polynomials with application to mammography," Med. Phys. 24, 1863–1874 (1997).

[14] J. M. Boone and J. A. Seibert, "An accurate method for computer-generating tungsten anode x-ray spectra from 30 to 140 kV," Med. Phys. 24, 1661–1670 (1997).

[15] J. M. Boone, "Spectral modeling and compilation of quantum fluence in radiography and mammography," Proc. SPIE 3336, 592–601 (1998).

[16] Los Alamos National Laboratory: http://mcnp-green.lanl.gov/

[17] H. Zaidi and M. Ay, "Current status and new horizons in Monte Carlo simulation of X-ray CT scanners," Med. Biol. Eng. Comput. 45, 809–817 (2007).

[18] Simulation of X-ray Spectra: https://w9.siemens.com/cms/oemproducts/Home/X-rayToolbox/spektrum/Pages/Default.aspx.

[19] K. Men, J. Dai, M. Li, and Y. Zhang, "A method to correct the influence of carbon fiber couchtop and patient positioning device on image quality of cone beam CT," Med. Phys. 37, 2466–2472 (2010).

[20] Y. Chen, B. Liu, J. M. O'Connor, C. S. Didier, and S. J. Glick, "Characterization of scatter in cone-beam CT breast imaging: Comparison of experimental measurements and Monte Carlo simulation," Med. Phys. 36, 857–869 (2009).

[21] H. Zaidi and B. H. Hasegawa, "Determination of the attenuation map in emission tomography," J. Nucl. Med. 44, 291–315 (2003).

[22] P. L. Chow, F. R. Rannou, and A. F. Chatziioannou, "Attenuation correction for small animal PET tomographs," Phys. Med. Biol. 50, 1837–1850 (2005).

[23] R. Prasad, M. R. Ay, O. Ratib, and H. Zaidi, "CT-based attenuation correction on the FLEX Triumph^{TM} preclinical PET/CT scanner," IEEE Trans. Nucl. Sci. 58, 66–75 (2011).

[24] J. H. Siewerdsen et al., "A simple, direct method for x-ray scatter estimation and correction in digital radiography and cone-beam CT," Med. Phys. 33, 187–197 (2006).